CuCrZr alloy produced by Laser Powder Bed Fusion: microstructure, nanoscale strengthening mechanisms, electrical and mechanical properties

Claudia Salvan, Laurent Briottet, Thierry Baffie, Laure Guetaz, Camille Flament

To cite this version:

Claudia Salvan, Laurent Briottet, Thierry Baffie, Laure Guetaz, Camille Flament. CuCrZr alloy produced by Laser Powder Bed Fusion: microstructure, nanoscale strengthening mechanisms, electrical and mechanical properties. Materials Science and Engineering: A, 2021, 826, https://doi.org/10.1016/j.msea.2021.141915. 10.1016/j.msea.2021.141915 . cea-03813244

CuCrZr alloy produced by Laser Powder Bed Fusion: microstructure, nanoscale strengthening mechanisms, electrical and mechanical properties

C. Salvan (Univ. Grenoble Alpes, CEA, LITEN, F-3800 Grenoble, France)
L. Briottet (Univ. Grenoble Alpes, CEA, LITEN, F-3800 Grenoble, France)
T. Baffie* (Univ. Grenoble Alpes, CEA, LITEN, F-3800 Grenoble, France)
*Corresponding author **thierry.baffie@cea.fr**
L. Guetaz (Univ. Grenoble Alpes, CEA, LITEN, F-3800 Grenoble, France)
C. Flament (Univ. Grenoble Alpes, CEA, LITEN, F-3800 Grenoble, France)

Published version available at: https://doi.org/10.1016/j.msea.2021.141915

Abstract

CuCrZr is a precipitation hardening alloy, used for its good electrical and thermal properties combined to high mechanical properties. Using additive manufacturing technologies, and more specifically the laser powder bed fusion (L-PBF) process, allows designing highly complex parts such as compact and efficient CuCrZr heat exchangers. Additional understanding of the specific CuCrZr metallurgy during this manufacturing process is still needed to fully take advantages of these possibilities. This work aimed (i) to clarify the impact of the L-PBF process and post-fabrication heat treatments on the microstructure of L-PBF CuCrZr alloy, (ii) to determine the corresponding mechanical and electrical properties and (iii) to quantify the contributions of the different nano-scale strengthening mechanisms (nano-precipitation, dislocations, solid solution, grain size refinement) depending on the different heat treatments. The microstructures of the CuCrZr samples are carefully analyzed at different scales thanks to scanning electron and transmission electron microscopy, highlighting the effect of the different heat treatments. In all heat-treated samples, Cr nano-precipitates are uniformly dispersed in the Cu matrix; few Zr nano-precipitates are observed either at grain boundaries, next to Cr nano-precipitates, or inside the Cu matrix. Moreover, the mean grain size, dislocation density, mean radius and volume fraction of the Chromium nano-precipitates are measured. These data are introduced in the identified hardening mechanisms to estimate the yield strengths (YS) of the different analyzed CuCrZr microstructures. The results are compared to the experimental values, including those of a reference wrought heat-treated CuCrZr, and discussed. A good correlation is found between calculated and experimental values. For the first time, the main hardening mechanisms of L-PBF CuCrZr are quantified and the interest of the “L-PBF+Direct Age Hardening (DAH)” process route to get a high amount of Cr nano-precipitates is confirmed. The DAH applied to L-PBF materials provides high mechanical properties (184 HV1 hardness, YS=527 MPa, UTS=585MPa) while keeping a good elongation (14%) and electrical conductivity (42 MS.m^{-1}). These results are due to a combination between (i) a high Cr nano-precipitates density, leading to a high precipitation hardening, and (ii) a high dislocation density associated to the presence of remaining solidification cells.

Keywords: Laser Powder Bed Fusion, mechanical properties, electrical properties, CuCrZr alloy, nanoscale strengthening mechanisms, heat treatments

1. Introduction

The Copper-Chromium-Zirconium (Cr: 0.5-1.2 wt.%; Zr: 0.03-0.3 wt.%) alloy is a precipitation-hardening alloy, which offers high electrical, thermal and mechanical properties. It is used, for example, in nuclear fusion reactor components as heat exchangers [1-2]. Laser Powder Bed Fusion (L-PBF) is a metallic additive manufacturing process, which has multiple advantages such as the ability to create easily complex shape components. It is used to build heat exchangers with small internal channels, improving their thermal exchange properties [1].

L-PBF process involves depositing a thin layer of metal powder that is melted by a laser according to a pattern defined by a *Computer Aided Design* (CAD) file. This operation is repeated to create a three-dimensional object.

Due to high optical reflectivity of copper-rich powders at the laser wavelength (1070 nm), several authors have studied the effect of coatings on Cu on CuCr powders, both for increasing absorption and forming in-situ alloys [3-5]. Even if this approach is effective in decreasing laser reflectivity, and thus the energy density required for melting the powder, neither Sn coating [3-4], nor Ni coating [3] lead to a final alloy as mechanically resistant as CuCrZr. The formation of a carburized layer at the surface of a CuCr powder, thanks to a nanometer carbon black powder deposition followed by a 750°C heat treatment [5], allowed to get relatively high tensile properties of L-PBF parts (Yield Strength YS = 347 MPa) after direct ageing, but this was only reached with a laser power over 400W. Indeed, CuCrZr gas-atomized powder can be processed efficiently in the 300-400W power range without costly additional powder modifications.

Despite the difficulties to process CuCr or CuCrZr alloy by L-PBF due to their high thermal conductivity and high optical reflectivity at 1070 nm [6], several recent studies [1,7-11] showed the ability to create dense CuCr and CuCrZr parts (relative density > 99%) in particular by using laser power over 300 W. Zeng et al. [11] studied the evolution of the Cu lattice parameter by X-rays diffraction (XRD) after heat treatments and the thermal properties of Cu-1.5Cr-0.5Zr alloy. This short communication only addresses the thermal properties; microstructures and mechanical properties were not deeply studied. The authors indicate that as-built L-PBF CuCrZr is not stable when re-heated and must be stabilized at temperatures above 500°C to form precipitates.

CuCr and CuCrZr wrought alloy needs to be heat-treated in order to induce the precipitation of nano-phases responsible for the hardening of the alloy. The different stages of heat treatments consist in a solution annealing (SA) of the Cr and Zr elements in the Cu matrix, followed by water quenching (WQ) leading to a supersaturated matrix. Finally, an age hardening (AH) treatment is necessary to precipitate (Cr, Zr) nano-phases in the matrix [12-13].

As the high cooling rate involved during the L-PBF process (of the order of 10^6 K/s) has the effect of quenching the microstructure, a direct age hardening (DAH) heat treatment can be applied to the as-built samples. Indeed, several studies [7,9,14] report that the L-PBF as-built

CuCr or CuCrZr alloys show no evidence of Cr or Zr precipitation at micrometric scale. More interesting, such a heat treatment leads to an increase of the Vickers hardness [7,9], the ultimate tensile stress (UTS) [7,14] and the electrical conductivity [7,14] with a thermal conductivity [9] comparable to that of wrought samples subjected to a conventional SA+AH heat treatment.

Zhang et al. [10] compared the effect of several heat treatments (SA between 900°C and 1020°C; SA at 1020°C + AH at 480°C; DAH at 480°C) on the lattice parameter, microstructure, mechanical properties, electrical properties and corrosion performances of Cu-0.5Cr alloy. Nano-precipitates were identified as nano-Cr face centered cubic (FCC) or body centered cubic (BCC) phases with specific orientation relationship as determined by Transmission Electron Microscopy (TEM)/selected area electron diffraction pattern. Concentrations of alloying elements in matrix range from 0.46 wt% in the as-built state, to 0.29 wt% in the SA+AH state and 0.03 % in the DAH, showing the interest of this last heat-treatment on the precipitation. The volume fraction of nano-precipitates varies from 0.05% in as-built state to 0.25 % in SA+AH state and up to 0.58 % in the DAH state. The experimental yield strength reaches 377 MPa after DAH, the elongation being 19% and the electrical conductivity 98 %IACS. The authors compared their YS experimental values to modelled ones using an addition of the different hardening contributions and experimental data from electron backscattered diffraction (EBSD) and TEM analyses; they found a good correlation.

Several studies dedicated to wrought CuCrZr alloy have shown that adding small amounts of zirconium to the Cu-Cr alloy plays a role in the precipitation of Cr and significantly increases the mechanical properties of the alloy [15-17]. With a small addition of Zr in a Cu-0.5Cr alloy, increases of 10 % on the yield strength and 6 % on the Vickers hardness are observed [17]. So, in a similar way as it was done by [10] for L-PBF Cu-Cr, there is an important interest to determine the contribution of each strengthening mechanisms in the case of a L-PBF CuCrZr alloy.

The main objective of the present work is to clarify the impact of the L-PBF process and post-fabrication heat treatments on the nano-scale microstructure of L-PBF CuCrZr alloy and the different strengthening mechanisms (related to nano-precipitation, dislocation strengthening, solid solution strengthening, grain size refinement). The understanding of these mechanisms are essential to be able to tailor the mechanical and electrical properties of the alloy to the targeted application. For this purpose, a study was performed to select the process parameters leading to the highest density. Then, scanning electron microcopy (SEM) associated to electron backscattered diffraction (EBSD) and transmission electron microscopy (TEM) associated to energy-dispersive X-rays spectroscopy (X-EDS) were used to characterize the samples microstructures. Vickers hardness and tensile tests were used to compare the mechanical properties, whereas eddy current measurements allowed determining the electrical properties. Based on EBSD and TEM analyses, mean grain size, dislocation density, mean radius and volume fraction of nano-precipitates were measured on the different heat-treated samples. Those measurements were used to calculate the yield strengths and compare them to the experimental YS values. The results obtained on L-PBF samples (As-built, SA+AH and DAH) were compared to those of a reference wrought SA+AH material. For the first time, the main hardening mechanisms of L-PBF CuCrZr are quantified and the interest of the “L-PBF+DAH” process route to get a high amount of chromium nano-precipitates is shown.

2. Materials and methods

2.1. Materials

L-PBF CuCrZr specimens were produced using a spherical 10-45 µm nitrogen-atomized powder (TLS Technik GmbH & Co). Chemical compositions of the powder, the L-PBF samples and the wrought CuCrZr plate, used as a reference, were measured by Instrumental Gas Analysis (IGA) and Inductively Coupled Plasma Optical Emission Spectroscopy (ICP-

OES) (Table 1). Chromium and zirconium contents in all samples are conform to the EN12420:2014 standard [18]. The iron content in the powder and the L-PBF samples is a bit higher than the minimum value expected by the standard.

Table 1: Chemical compositions of CuCrZr powder upon receipt, L-PBF CuCrZr and wrought CuCrZr samples compared to standard (values correspond to the average of three measurements).

Element [wt.%]	**Cr**	**Zr**	**Fe**	**Si**	**O**	**Others**	**Cu**
CuCrZr - EN12420:2014 standard	0.5-1.2	0.03-0.3	< 0.008	< 0.1	< 0.2		*Bal.*
Wrought CuCrZr (reference)	0.596 ± 0.014	0.071 ± 0.001	0.004 ± 0.001	<0.002	0.005 ± 0.001	-	*Bal.*
Powder upon receipt	0.751 ± 0.01	0.086 ± 0.002	0.020 ± 0.001	0.005 ± 0.002	0.018 ± 0.002	0.02	*Bal.*
L-PBF CuCrZr (studied material)	0.781 ± 0.012	0.088 ± 0.003	0.029 ± 0.001	0.008 ± 0.005	0.012 ± 0.001	-	*Bal.*

2.2. L-PBF specimens

All specimens were produced on a FS271 L-PBF device (Farsoon, China). The device is equipped with a 480 W fiber laser with a wavelength of 1070 nm and a 130 µm Gaussian spot diameter. The powder was handled in a glovebox, dried before L-PBF and the oxygen level was maintained below 250 ppm during the whole fabrication process. During the process, the powder was spread using a silicon blade, and the specimens were produced on a 270 mm x 270 mm C45 steel platform. The layer thickness was set to 30 µm. A zigzag laser strategy on 10 mm wide stripes, forming a 45° angle with the cubes or pieces edge, with a 90° rotation between layers was used. The chamber was filled with argon gas. Cubes (10x10x10 mm^3, Figure 1.b) were built with a different set of parameters and the resulting density was measured. Their base was rotated 45° with respect to the blade path. The laser power (P) varied from 360 to 480 W, the scan speed (v) from 200 to 700 mm.s^{-1} and the hatch (h) from 100 to 120 µm. The optimized parameters, i.e. the parameters that lead to the highest density (99.4%), are a power of 480 W, a scan speed of 700 mm.s^{-1} and a hatch of 100 µm (Figure 1.a). Those parameters were then used to fabricate mechanical and electrical samples (Figure 1.c). 55x13x13 mm^3 parallelepipeds were built for mechanical samples; their small bases was rotated 45° in the YZ plane and their main axis was rotated 45° relative to the direction of the blade. 18 mm diameter and 22 mm high cylinders were built for electrical samples.

2.3. Material characterization techniques

The density of L-PBF CuCrZr was measured on polished samples (SiC P320), by Archimedes method using isopropanol thanks to the equation (1) :

$$\rho_{\text{relative density}} = \frac{M_{\text{L-PBF sample}}}{M_{\text{HIP}}} \tag{1}$$

where $M_{L-PBF\ sample}$ is the density of L-PBF CuCrZr, M_{HIP} is the density of Hot Isostatically Pressed (HIPed) CuCrZr samples obtained by HIPping the CuCrZr powder at 1040°C for 2 hours under 1400 bar; their density was measured with helium pycnometer on an AccuPyc II 1340 Micrometrics and used as a reference. The standard deviation on the relative density is ±0.25%. The chemical composition was verified by IGA and ICP-OES on three different parts for each CuCrZr (Table 1). The SA + AH heat treatments have been applied to L-PBF and wrought samples. They consist in a solution annealing followed by water quenching (WQ), and subsequent thermal ageing under air followed by air-cooling (Table 2). The temperature and exposure time were chosen according to previous research on this material for fusion nuclear reactor applications [19-20]. A DAH heat treatment, which consists in an age hardening under air followed by air-cooling [9] (Table 2), has been applied to as-built L-PBF samples. This heat treatment corresponds to the best compromise between mechanical and thermal properties according to [9].

Table 2: Heat treatments applied to the CuCrZr samples

Heat treatment	Temperature [°C] / Atmosphere	Exposure time [min]	Cooling type	Samples concerned
Solution Annealing + Age Hardening (SA+ AH)	980 / Ar + 490 / Air	60 + 360	Water quenching + Air cooling	L-PBF Wrought

Direct Age Hardening (DAH)	490 / Air	60	Air cooling	L-PBF

For the SEM and TEM observations, samples were cut normal to the building direction (noted ⊙ BD plan in Figure 2) or parallel to the building direction (noted ↑ BD plan in Figure 2). The plates were mechanically polished down to 100 µm thickness, punched out into 3 mm disks and electro-polished. The electro-polishing was performed at room temperature with a solution of 25 vol.% ethylene glycol, 25 vol.% ortho-phosphoric acid and 50 vol.% deionized water at 20°C, under an applied potential of 12 V, and with a 200-300 mA current. For SEM analysis, the electro-polishing was stopped quickly, to remove hundreds of nanometers of damaged surface. For TEM analysis, the electro-polishing was carried on to obtain a thickness of around 20 µm. The disks were then polished using an argon ion beam polishing (PIPS 2 GATAN 691) to create a hole and avoid oxidation issues observed after an electro-polishing.

SEM observations were performed on a field emission gun (FEG) SEM Zeiss Merlin equipped with two Energy Dispersive Spectroscopy (EDS) detectors and an Electron Back-scattered Diffraction (EBSD) QUANTAX detector from Bruker. EBSD analyses using Esprit 2.2 software for data processing were used to assess the average grain size and the median misorientation angle. Grains boundaries are defined with a misorientation angle higher than 15° and subgrains boundaries with a misorientation angle lower than 15°. The grain size is defined as the equivalent diameter of a circle of the same surface as the observed grains. The average grain size is weighted by the surface. A Kernel Average Misorientation map (KAM) analysis, which measures the local misorientation of a pixel between 0.5° and 5° against the closest pixels, was used to define the median misorientation angle. This angle (θ [rad]) is then used to estimate the dislocation density (ρ_0) thanks to equation (2) [21].

$$\rho_0 = \frac{2\sqrt{3}}{3}\frac{\theta}{bs} \tag{2}$$

With b [m], the Burgers vector and s [m] the step size used during the EBSD analysis. The Burgers vector is taken equal to 0.256 nm for a Cu matrix [12].

TEM analyses were performed on a TITAN Themis (FEI), operating at 200kV and equipped with a Cs probe corrector, a Super-X system (4 Silicon Drift Detectors) for EDS analyses and a Gatan Imaging Filter (GIF Quantum) for Electron Energy Loss Spectroscopy (EELS) analysis. Images were acquired in scanning transmission electron microscopy (STEM) mode using either a HAADF (high angle annular dark field) or a BF (bright field) detector.

2.4. Mechanical and electrical analyses

Vickers hardness was measured on a Matsuzawa MMT-X7B micro-hardness tester according to EN ISO 6507-(1-4) [22] with a load of 1 kg during 15 seconds; 10 indents were made per sample. Tensile tests perpendicular to the building direction were done on 3 specimens per CuCrZr state under air, at 20°C on a MTS servo-hydraulic testing machine with a 100 kN load cell at a 2.5×10^{-4} s^{-1} strain rate. Tensile bars were made according to NF EN ISO 6892-1 [23]. Electrical conductivity was measured, according to EN 2004-1 standard [24], at 20°C on 3 polished specimens per CuCrZr state (SiC P4000), by Eddy current on a Fischer FS40 machine.

3. Experimental results

3.1. Relative density and chemical composition

Figure 1.b shows the cubic L-PBF specimens. Their relative density as a function of the energy density Ev [$J.mm^{-3}$] input during the process is presented in Figure 1.a. Ev depends on the laser power energy P [W], the laser scanning velocity v [$mm.s^{-1}$], the hatch h [mm] and the layer thickness l [mm], as given in equation (3) [25-26].

$$E_v = \frac{P}{v * h * l} \tag{3}$$

The relative density of the alloy increases with increasing Ev input. A minimum Ev of approximatively 300 $J.mm^{-3}$ is needed to achieve a relative density equal to or higher than 99%. At a laser power of 360 W, only a few sets of parameters leading to a high Ev with small scan speeds (200 and 300 mm.s^{-1}), offer a relative density higher than 99%. Whereas, 480 W laser power offers the widest range of Ev which can achieve a relative density higher than 99% even with a laser speed of 700 mm.s^{-1} that allows higher productivity. Consequently, a laser power of 480 W, a scan speed of 700 mm.s^{-1} and a hatch of 100 µm were used for building the samples of this work.

The chemical composition of the samples is comparable to that of the powder (Table 1). The oxygen content is stable, showing no evidence of oxidation during the process. In addition, no evidence of impurities, cross contamination, or Zr loss, was detected.

3.2. Microstructure of the L-PBF as-built CuCrZr

Figure 3.a and Figure 3.d show SEM images of the L-PBF as-built CuCrZr taken in the ⊙ BD and ↑ BD plans respectively. Figure 3.b and Figure 3.e are EBSD quality patterns images superimposed with grain and subgrain boundaries defined by different misorientation angles. The microstructure is anisotropic. In the ↑ BD plan, grains are elongated along the BD direction (Figure 1.d-e). The average grain size is 217 ± 80 µm (363 ± 160 µm long and 125± 60 µm width). The grain cross-sections form a pavement in the ⊙ BD plan (Figure 3.b). This particular shape is due to the combination of the spot size and the zigzag scan strategy [25]. The grains have a nearly squared shape, 100 µm side, and in some cases, are elongated at 60° in regards to the scan path direction. The average grain size in this plane is 115 ± 60 µm. A large number of subgrains (misorientation angle <15°) are observed, they are distributed with high and low density zones. These zones are also highlighted on the KAM map that image the local misorientation (Figure 3 c).

Inside the subgrains, TEM observations revealed the presence of dislocation cells having an average size of 300 nm (Figure 3f). They probably are solidification cells resulting from the high solidification rate of the L-PBF process and are observed on other L-PBF alloys [27].

KAM analysis is used to estimate the dislocation density in the CuCrZr (equation (1)). The measurement was performed at two different magnifications: at low magnification, which underestimates the dislocation density but provides an average dislocation density in this non-homogeneous CuCrZr, and at high magnification, with a step size of 0.1 µm that is smaller than the solidification cells (300 nm) for a more relevant estimation. These values are used to compare the different metallurgical states and the results are reported in Table 4. The as-built CuCrZr presents a high dislocation density ($5 \pm 1 \times 10^{14}$ m^{-2}), comparable to the dislocation density obtained on cold worked CuCrZr (5×10^{14} m^{-2}) [28]. The dislocations appear during the L-PBF process due to high stresses induced by the thermal gradients generated during the rapid solidification. The thermal history of the CuCrZr during the process is complex and inhomogeneous, and so is the microstructure.

3.3. Effect of the heat treatment on L-PBF CuCrZr and comparison with wrought CuCrZr

Figure 4 shows the SEM and EBSD microstructures of the wrought and the different L-PBF heat-treated CuCrZr (heat treatments are reported in Table 2). The wrought SA+AH CuCrZr whose microstructure (Figure 4.a and d) is different to the L-PBF alloy, shows large equiaxed grains with numerous twins, leading to an average grain size (including twins) of 470 ± 150 µm (Table 3). A dislocation density of 3×10^{13} was estimated using KAM analysis (Table 5). This density is similar to the value found by [28] on wrought Cu-0.8Cr-0.1Zr (wt.%) in the same metallurgical state.

For the L-PBF alloy, the SA + AH heat treatment caused an evolution of the microstructure (Figure 4.b and e) compared to the as-built state (Figure 3). The pavement shape of the grain cross-section in the ⊙ BD plan and the elongated grain cross-section in the ↑ BD plan is partially preserved however in some area, recrystallization has occurred and has resulted in larger twinned grains. The average grain size is 276 ± 150 µm in the ⊙ BD plan and 334 ± 140 µm in the ↑BD plan (Table 3). This partial recrystallization (60% of the surface) is confirmed by the KAM analysis (Figure 4.g). No solidification cells are observed in both, recrystallized or non-recrystallized grains. The dislocation recovery should occur prior to the recrystallization during the 980°C SA heat treatment. Given the absence of solidification cells, a step size of 1.7 or 2.1 µm was used for KAM analysis to estimate the dislocation density (Table 4). Dislocation density in the recrystallized zones is found to be close to the value of the wrought SA+AH CuCrZr ($3 \pm 1 \times 10^{13}$ m^{-2}), while in the non-recrystallized zone it is higher ($7 \pm 1 \times 10^{13}$ m^{-2}).

Table 3 : Average grain size of the different CuCrZr samples.

CuCrZr	**L-PBF DAH**		**L-PBF SA+AH**		**Wrought SA+AH**
	⊙ BD	**↑BD**	**⊙ BD**	**↑ BD**	
Average grain size [µm]	112 ± 60	242 ± 100	276 ± 150	334 ± 140	471 ± 150
Number of grains counted	785	368	338	406	44

On the contrary, the DAH heat treatment involved no change of grain morphology and size compared to the as-built state (Figure 4.c and f), a similar average grain sizes of 112 ± 60 µm, in the ⊙ BD plan and 242 ± 100 µm in the ↑ BD plan were measured (Table 3). Moreover, the dislocation cells with similar size as the as-built state were still observed by TEM. It is however likely that the heat treatment at 490°C allows a dislocation recovery in the cell walls that can explain the slightly lower dislocation density measured by KAM analysis (Figure 4.h) than in the as-built state (4×10^{14} m^{-2} versus 5×10^{14} m^{-2}) although this difference is within the measurement error bar.

Table 4 : KAM median misorientation angle θ and average dislocation density ρ_0 as a function of the step size used s, estimated for L-PBF as built, L-PBF SA+AH and L-PBF DAH, and wrought SA+AH CuCrZr alloys.

CuCrZr	**Analysed surface**	**Cells size [nm]**	**s [µm]**	**θ [°]**	**ρ_0 [m^{-2}]**
L-PBF as-built	1 cm^2	300	2.0	1.9	$8 \pm 1 \times 10^{13}$
	4.5 mm^2		0.1	0.7	$5 \pm 1 \times 10^{14}$
	1 cm^2	No cell	1.7	0.9	$4 \pm 1 \times 10^{13}$

L-PBF SA+AH	0.6 cm^2 (recrystallized zone)		1.7	0.7	3 ± 1 x 10^{13}
	0.4 cm^2 (non-recrystallized zone)		1.7	1.5	7 ± 1 x 10^{13}
L-PBF DAH	1 cm^2	330	2.3	2.2	7 ± 1 x 10^{13}
	4.5 mm^2		0.2	0.7	4 ± 1 x 10^{14}
Wrought SA+AH	1 cm^2	No cell	2.1	0.7	3 ± 1 x 10^{13}

3.4. Micro- and nano-precipitation

In the as-built L-PBF CuCrZr, Cr, and Zr micro- or nano-precipitates are not detected (Figure 5.b and Figure 6.a), which confirms that Cr and Zr form a solid solution in the Cu matrix of this material. After heat treatment and due to the low solubility of the Cr and Zr in the copper matrix, Cr and Zr form micro or nano-precipitates.

Cr micro-precipitates were observed on SEM images (Figure 5). In the wrought SA+AH CuCrZr, they are intragranular precipitates (Figure 5.a). In contrast, in the L-PBF SA+AH CuCrZr, they are intergranular or located along sub-grain boundaries in the non-recrystallized areas, but they are also intragranular in the recrystallized areas (Figure 5.d). Contrary to SA+AH, the DAH heat treatment did not induce Cr micro-precipitation (Figure 5.c). Thus, during the DAH heat treatment, a larger amount of Cr was involved in the nanoprecipitation as confirmed in the following.

Zr nano-precipitates are observed in different locations and with different shapes after SA+AH or DAH heat treatments: at grain boundaries, next to Cr nano-precipitates (the Zr precipitate size is then between 5 and 30 nm as in Figure 6.d), inside the Cu matrix (Zr hexagonal precipitate with 10-40 nm of diameter). EDS analyses of these Zr nano-precipitates show a particularly high Cu peak suggesting these precipitates could be Cu_5Zr or Cu_4Zr according to [12].

The Cr nano-precipitates were observed in all heat-treated CuCrZr samples; they are uniformly dispersed in the Cu matrix (Figure 6.b and c), and display an ellipsoidal shape (Figure 6.e and f). They have a face centered cubic (FCC) structure and are coherent with the matrix. In the wrought SA+AH CuCrZr, the equivalent radius (r) is uniform at 1.8 ± 1.0 nm (Table 5). In the L-PBF DAH CuCrZr, r varies depending on the nano-precipitate location. For the precipitates, which have grown on dislocations or grain boundaries, it is around 3.2 ± 1.6 nm, whereas for one located in the Cu matrix it is around 2.1 ± 1.5 nm (Table 5). This could be explained by a specific precipitation occurring at the grain boundaries in DAH CuCrZr. Note the equivalent radius measurement gives a high standard deviation.

Table 5 : TEM analysis of the equivalent radius and volume fraction of Cr nano-precipitates on heat treated CuCrZr.

CuCrZr	**Equivalent radius [nm]**	**Number of precipitates measured**	**Volume fraction of precipitates [%vol]**
L-PBF DAH	2.1 ± 1.5	233	0.6
Wrought SA+AH	1.8 ± 1.0	54	0.3

To determine the volume fraction of the precipitates, the thickness of the CuCrZr thin foils where TEM analysis was performed was roughly estimated by EELS at 30 nm. Considering this value, the volume fraction of the Cr nano-precipitates in the CuCrZr matrix of the L-PBF DAH CuCrZr was estimated (3 images were analyzed) to be 0.6 % (Table 5). This is consistent with the theoretical volume fraction of Cr in solid solution in the L-PBF as built CuCrZr which is 0.62 vol% (estimation made with the chemical composition of Table 1, and thanks to the theoretical density of Cu, Cr and Zr [29]). Then the volume fraction of Cr nano-precipitates is twice higher in the L-PBF DAH CuCrZr than in the wrought SA+AH CuCrZr (Table 5). As the size of the precipitates in both L-PBF DAH and wrought SA+AH CuCrZr is equivalent, the number of precipitates is lower, and thus the distance between them is greater in the L-PBF DAH CuCrZr.

3.5. Mechanical properties

HV1 Vickers hardness performed on the different materials are presented in Table 6 and, as indicated by the standard deviation, the hardness testing has good repeatability. The hardness of the as-built L-PBF CuCrZr is 101 ± 4 HV1, which is close to the values found by [7,9] for similar process parameters. This obtained value is high compared to that of the CuCrZr (SA+WQ) from literature (65-77 HV1 [30]), which is also a microstructural state free from nano-precipitates. Hardness was found to be similar for L-PBF SA+AH and wrought SA+AH CuCrZr tested here and compared to similar CuCrZr SA+AH from the literature [8-9,12,20]. This is probably due to the recrystallization occurring during the SA heat treatment. By contrast, the L-PBF DAH CuCrZr hardness is much higher than the others, in agreement with literature [7,9].

Table 6: Tensile and hardness properties of wrought SA + AH, L-PBF as-built, L-PBF SA + AH and L-PBF DAH CuCrZr tested at 20°C.

CuCrZr	**YS**	**UTS**	**Total Elongation**	**Vickers Hardness**
	[MPa]	**[MPa]**	**[%]**	**[HV1]**
L-PBF As-built (⊙ BD)	270 ± 6	305 ± 5	26 ± 2	101 ± 4
L-PBF SA + AH (⊙ BD)	253 ±8	380 ± 7	25 ± 2	112 ± 5
L-PBF DAH (⊙ BD)	527 ± 3	585 ± 1	14 ± 1	184 ± 4
Wrought SA + AH	221 ± 1	349 ± 3	33 ± 1	116 ± 2

Figure 7 shows tensile test curves for the different alloys recorded at 20°C (as the curves were qualitatively similar, only one for each condition is shown on the graph). The yield strength, ultimate strength and the elongation values are given in Table 6. The low elongation observed on the L-PBF SA+AH or DAH CuCrZr compared to wrought SA+AH CuCrZr (tested here, or from the literature [20]) can be explained by the residual porosity of the L-PBF CuCrZr samples, identified by the presence of few unmelted particles found on the fractography (Figure 7.b). The ultimate tensile strength (UTS) and the yield strength (YS) of the L-PBF SA+AH CuCrZr are slightly greater than the wrought CuCrZr ones. The L-PBF DAH CuCrZr has different mechanical behavior: an elongation half as high as wrought SA+AH CuCrZr and a YS 95% higher, even higher than the L-PBF DAH CuCrZr of [14]. A limited strain hardening is also observed on the L-PBF DAH CuCrZr. The presence of cells and extremely high dislocation density in L-PBF DAH CuCrZr is probably due to an equilibrium between creation and annihilation of dislocations, which explains the shape of the curves. Moreover, in all tested samples (Figure 7.c), dimples are visible on the fracture surface.

3.6 Electrical properties

The low electrical conductivity of L-PBF as-built CuCrZr is consistent with a supersaturated solid solution state of the Cu matrix (Table 7) and the observations made in ref [7]. After SA+AH, both the L-PBF and wrought CuCrZr samples show similar electrical conductivity, even compared to the wrought SA+AH from literature [20]. Finally, L-PBF DAH CuCrZr displays a lower conductivity compared to SA+AH samples, due to the still high amount of dislocation density [31]. This tendency is in agreement with the values of other studies [7,14].

Table 7: Electrical conductivity measured by Eddy current

CuCrZr	**Electrical Conductivity**
	[10^6 S.m^{-1}]
L-PBF As-built (⊙ BD)	14.3 ± 0.1
L-PBF SA + AH (⊙ BD)	51.1 ± 0.1
L-PBF DAH (⊙ BD)	41.6 ± 0.4
Wrought SA + AH	51.9 ± 0.3

4. Discussion

4.1. Microstructural evolution of L-PBF CuCrZr

During L-PBF process, the heat transfer through the already densified part tends to create elongated grains in the building direction. Gorsse et al. [25] found similar grain morphology, i.e. elongated grains in the ↑BD plan and pavement of the size of the laser hatch in the ⊙ BD plan. Moreover, a cellular growth is observed due to high cooling rate typical of materials fabricated by L-PBF [25,27]. This leads to a high dislocation density present in the as-built part. They do not show any evidence of micro- or nano-precipitates (Figure 8). The solubility limit of Cr is then 0.78 wt.%, more than the theoretical solubility limit of Cr in Cu-Cr alloy (0.72 wt.% [32]).

After SA+AH on L-PBF CuCrZr, recrystallization is observed on 60% of the surface. During SA, at 980°C, partial recrystallization is possible, as shown by [33] on cold rolled wrought CuCrZr. In the recrystallized zones, the microstructure is similar to the wrought CuCrZr, with large twined grains showing no particular orientation. After WQ of the SA treatment, the Cr and the Zr partially precipitate at a micrometric scale and are partially maintained in solid solution (0.4 wt.% maximum [32]) (Figure 8). The AH treatment allows the Cr and Zr in solid solution to precipitate at a nanometric scale (Figure 8).

After DAH, the specific microstructure of L-PBF as-built CuCrZr is globally preserved. A slight dislocation recovery is observed, but the solidification cells remain. The age hardening temperature (490°C) is not high enough to trigger recovery. All the Cr, which was in a supersaturated solid solution state, precipitates at a nanometric scale, leading to a volume fraction of nano-precipitates twice as high as after SA+AH (Figure 8).

4.2. Hardening mechanisms

In the following, the different hardening mechanisms acting on the mechanical behavior of our four samples will be estimated, to discuss the effect of the processes and heat treatments. The yield strength (YS) of such materials depends on several contributions according to equation (4) [10,34-35].

$$YS = \sigma_0 + \Delta\sigma_{ss} + \Delta\sigma_{gs} + \Delta\sigma_{ds} + \Delta\sigma_{ps} \tag{4}$$

With σ_0 the friction lattice or Peierls-Nabarro stress, $\Delta\sigma_{ss}$ the solid solution strengthening, $\Delta\sigma_{gs}$ the grain size refinement contribution, $\Delta\sigma_{ds}$ the dislocation strengthening and $\Delta\sigma_{ps}$ the precipitation strengthening. To investigate the increase of YS observed in the L-PBF CuCrZr, and especially in the DAH CuCrZr, each contribution is individually examined for the four metallurgical states in the following sections. Some parameters have been evaluated experimentally whereas the others have been taken from the literature (Table 8).

Table 8: Value of the parameters for pure Copper used in the calculations

Parameters		Value	Unit	Reference
σ_0	Peierls-Nabarro stress	20	MPa	[16]
G	Shear modulus of the matrix	45.5	GPa	[34,36-37]
k	Hall Petch slope	180	MPa.µm$^{1/2}$	[16,34]
M	Taylor factor	3.06	-	[10,28,36]
b	Burgers vector	0.256	nm	[12,36]
α	-	0.23	-	[10]
ε	Misfit	0.015	-	[14,38]
ν	Poisson’s ratio	0.34	-	[34,39]

4.2.1. Solid solution strengthening

The elements remaining in solid solution in the Cu matrix can play a strengthening effect caused by the induced crystal lattice distortion affecting dislocation movement (equation (5)) [10]:

$$\Delta\sigma_{ss} = MG\varepsilon^{3/2}\sqrt{\frac{x_a}{3}} \tag{5}$$

With $x_a[wt.\%]$ the mass concentration of the element in the solid solution. The Zr, O, Si and Fe contributions are neglected due to their low content and low solubility limits in the Cu matrix [40].

In the as-built L-PBF CuCrZr, all Cr atoms are in solid solution (x_a is then equal to 0.78 wt.%, Table 1), as no evidence of precipitation has been found during TEM observations. Thus, the contribution of solid solution strengthening to YS is 35 MPa. After SA+AH or DAH, nearly all Cr atoms have precipitated as the electrical conductivity proves. We decided to discard this contribution for these heat treatments. Indeed, even with 10 wt.% of the total content of Cr in solid solution, this contribution would represent less than 10 MPa.

4.2.2. Grain size

The contribution of the grain size to the YS is given by the Hall-Petch model (6) [41-42].

$$\Delta\sigma_{gs} = \frac{\mathrm{k}}{\sqrt{\mathrm{D}}} \tag{6}$$

With D [µm] the average grain size. As shown in Figure 3, the grains of L-PBF CuCrZr are columnar. Thus, an assumption has been made on the grain size. We decided to take the critical situation and thus consider the smallest grain size, i.e. in the ⊙ BD plan. In addition, twins appear in the SA+AH CuCrZr. As twins also impede the dislocation motion, they have been considered as grain boundaries, lowering the values given in Table 3. The calculated $\Delta\sigma_{gs}$ for the different CuCrZr are reported in Table 9. The twins in SA+AH CuCrZr do not affect significantly the grain contribution to YS. Whatever the metallurgical state, the grain size contribution to the YS is low and accounts for 3% to 8% of the total YS.

Table 9: Grain size contribution, dislocation density measured thanks to KAM analysis, dislocation strengthening contribution in the different CuCrZr, channel size between the nano-precipitates and strengthening contribution for the different CuCrZr.

CuCrZr	**L-PBF As-built**	**L-PBF DAH**	**L-PBF SA+AH**	**Wrought SA + AH**
Average equivalent grain diameter [µm]	115 ± 60	112 ± 55	80 ± 40	186 ± 108
Number of grains	902	785	1095	514
$\Delta\sigma_{gs}$ [MPa]	17	17	20	13
ρ_0 [m^{-2}]	5 ± 1 x10^{14}	4 ± 1 x10^{14}	4 ± 1 x10^{13}	3 ± 1 x10^{13}
$\Delta\sigma_{ds}$ [MPa]	184	153	52	41
L_p [nm]	Ø	36	Taken equal to wrought SA+AH values	45
$\Delta\sigma_{ps}$ [MPa]	Ø	402		304

4.2.3. Dislocation strengthening

The dislocation strengthening mechanism, due to the dislocation forest effect, can be estimated in an isotropic material thanks to equation (7) [28,43] (the heterogeneous distribution of dislocation density is neglected).

$$\Delta\boldsymbol{\sigma}_{ds} = \alpha M G b\sqrt{\rho_0} \tag{7}$$

With ρ_0[m^{-2}] the dislocation density, measured by KAM analysis (section 3.2 and Table 4). The dislocation strengthening magnitude depends on the process and the applied heat treatment (Table 9). On a wrought SA+AH CuCrZr, this contribution to the YS is low, since the heat treatment leads to a rather low dislocation density. By contrast, it is 4.5 times higher for the as-built L-PBF sample due to the high dislocation density induced by the high cooling rate. The SA part of the SA+AH strongly decreases the dislocation strengthening contribution to YS. The remaining non-recrystallized grains in this sample however contribute to an intermediate dislocation strengthening, which is 25% higher than the one of wrought SA+AH. With the DAH, the dislocation density slightly decreases due to a slight recovery of the dislocations located on the solidification cells walls. However, this contribution is 3.7 times higher than the one of wrought SA+AH.

4.2.4. Precipitation strengthening

In this part, we assumed that precipitation strengthening is driven by the Orowan-Ashby mechanism [12,28,44] which strongly depends on the channel size between the nano-precipitates, directly related to the duration and temperature of the age hardening step. The smaller this length, the harder it is for the dislocations to curve and to cross the precipitates. This impedes the dislocation motion and hardens the alloy. The contribution of the nano-precipitation to the YS is estimated using equation (8) [39,43,45].

$$\Delta\sigma_{ps} = \frac{0.8 * \mathrm{M}Gb}{2\pi\sqrt{1-\nu}} \cdot \frac{ln\left(\frac{2\mathrm{r}}{\mathrm{r}_0}\right)}{L_p} \; with \; L_p = r\left(\sqrt{\frac{2\pi}{3f}} - \frac{\pi}{2}\right) \tag{8}$$

The 0.8 factor is a statistic factor, reflecting the random repartition of the precipitates in the slip plan [46]. With r [nm] the mean radius of the nano-precipitates, r_0 [nm] the cut-off radius or radius of dislocation core, that can be taken equal to the Burgers vector [45], L_p [nm] the channel size between the nano-precipitates and f the volume fraction of precipitates. As the quantity of Zr nano-precipitates in the Cu matrix is low, only the Cr nano-precipitation is taken into account to estimate this contribution. r and f have been measured by TEM (Table 5). Moreover, we assume that the L-PBF and wrought CuCrZr have the same Cr nano-precipitation after the SA+AH heat treatments.

The calculated precipitation strengthening contribution (Table 9) is overestimated as the experimental YS does not exceed 300 MPa (Table 6). This overestimation can come from the imprecise determination of precipitates size (50% inaccuracy due to high standard deviation, Table 5. Some high resolution TEM analyses made on the size of precipitate (Figure 6.e-f) seem to confirm the underestimation of the radius. It is also possible that a shear hardening mechanism is acting instead of the Orowan hardening mechanism. Nevertheless, the obtained trends are consistent: this contribution is predominant in all heat-treated CuCrZr, and the biggest in the L-PBF DAH CuCrZr. Such a heat treatment provides a high nano-precipitation density in the Cu matrix reducing the average channel size, and thus increasing the precipitation strengthening contribution.

4.2.5. Comparison between the experimental YS and the calculated YS contributions

The objective of the previous calculations was to quantify the contribution of the different nano-scale strengthening mechanisms (nano-precipitation, dislocations, solid solution, grain size refinement) for each CuCrZr sample (L-PBF as-built, L-PBF SA+AH, L-PBF DAH and the reference wrought SA+AH). Some interesting results emerge from this analysis. Figure 9 summarizes the different contributions to the YS calculated for each heat-treated CuCrZr and compared to the experimental YS (black spots). Qualitatively, we found the right trends for every metallurgical states. In the L-PBF SA+AH and wrought SA+AH CuCrZr, the predominant strengthening mechanism is the nano-precipitation strengthening, accounting for, respectively, 80% and 85% of the total strengthening. The overestimation of 48% to 62% of the calculated YS compared to the experimental one, respectively for the L-PBF SA+AH and wrought SA+AH CuCrZr, can come from the high standard deviation on the mean radius of the Chromium nano-precipitates. For the as-built L-PBF CuCrZr, there are two main acting mechanisms: dislocation strengthening (78% of calculated YS) and solid solution strengthening (15% of calculated YS). The difference between the measured and estimated YS is less than 15%. For the L-PBF DAH CuCrZr, the precipitation strengthening and the dislocation strengthening account, respectively, for 70% and 27% of the total estimated YS. The difference between the measured and estimated YS is less than 8%. Thus, the supersaturated Cu solid solution obtained thanks to L-PBF process offers the possibility to precipitate more nano-Cr after a DAH (0.6 %vol. as shown in Figure 8) than what is possible with a SA+AH (0.3 %vol.), increasing the precipitation strengthening.

5. Conclusions

In this study, we have shown that:

(1) CuCrZr samples with a relative density higher than 99% have been successfully processed by L-PBF.

(2) the L-PBF as-built CuCrZr alloy microstructure shows columnar grains, a high dislocation density due to the presence of solidification cells of 294 ± 32 nm of diameter, and it is in a supersaturated state without Cr micro- nor nano-precipitate, which is very different from the well-known wrought CuCrZr alloy. In L-PBF as-built sample, the volume fraction of Cr in solid solution is twice the one of the SA+WQ wrought alloy; this is explained by the higher cooling rate of the L-PBF process.

(3) Applying a solution annealing at 980°C for 1h followed by an ageing at 490°C for 6h on a L-PBF CuCrZr sample recrystallizes the microstructure at 60%. During the solution annealing, a part of the Cr (0.4 wt%) forms micro-precipitates while the other part

remains in solid solution which will form nano-precipitates after the age hardening treatment. The mechanical properties are comparable to wrought CuCrZr in the direction perpendicular to the building one.

(4) A direct ageing at 490°C for 1 hour allows to precipitate all the Cr (0.78 wt%) at nanometric scale but does not modify the microstructure of the as built L-PBF CuCrZr (columnar grain, high dislocation density) to a huge extent. This particular heat treatment offers high mechanical properties (Vickers hardness of 184 HV1, YS=527 MPa and UTS=585 MPa) while conserving a significant elongation (14%) and good electrical properties (42 MS.m^{-1}) compared to SA+AH heat treatments. This is due to the high dislocation density and the high Cr nano-precipitates density, which lead to a lower distance between precipitates and a stronger structural hardening compared to the one after SA+AH.

Further investigations on the SA+AH heat treatment on L-PBF CuCrZr may offer the possibility to get totally rid of the anisotropic microstructure induced by the process. A further investigation on the DAH heat treatment may offer the possibility to determine precisely the hardening peak depending on the Cr concentration in the alloy. A TEM study of the Cr nano-precipitates on CuCrZr tensile samples may confirm the structural hardening mechanism (shear or bypass mechanism) playing a role here.

Data availability

The raw/processed data required to reproduce these findings cannot be shared at this time as the data also forms part of an ongoing study.

Acknowledgments

The authors gratefully acknowledge CEA-LITEN and the CARNOT “Energies du Futur” program for their financial support. The TEM and SEM measurements were performed at the

CEA NanoCharacterization Platform (PFNC) - Minatec, supported by the French RTB (IRT Nanoelec) and the equipex NanoIDT. The authors also gratefully thanks T. Germain, B. Riccetti, M. Pellat and P.E. Frayssines for their help in this work.

References

[1] Z. Ma, K. Zhang, Z. Ren, D. Z. Zhang, G. Tao, and H. Xu, “Selective laser melting of Cu–Cr–Zr copper alloy: Parameter optimization, microstructure and mechanical properties,” *Journal of Alloys and Compounds*, vol. 828, no. 154350, Art. no. 154350, Jul. 2020, doi: 10.1016/j.jallcom.2020.154350.

[2] S. J. Zinkle, “Applicability of copper alloys for DEMO high heat flux components,” *Phys. Scr.*, vol. 2016, no. T167, Art. no. T167, 2016, doi: 10.1088/0031-8949/2015/T167/014004.

[3] V. Lindström *et al.*, “Laser Powder Bed Fusion of Metal Coated Copper Powders,” *Materials*, vol. 13, no. 16, Art. no. 16, Aug. 2020, doi: 10.3390/ma13163493.

[4] S. D. Jadhav *et al.*, “Highly conductive and strong CuSn0.3 alloy processed via laser powder bed fusion starting from a tin-coated copper powder,” *Additive Manufacturing*, vol. 36, p. 101607, Dec. 2020, doi: 10.1016/j.addma.2020.101607.

[5] S. D. Jadhav *et al.*, “Laser powder bed fusion additive manufacturing of highly conductive parts made of optically absorptive carburized CuCr1 powder,” *Materials & Design*, vol. 198, p. 109369, Jan. 2021, doi: 10.1016/j.matdes.2020.109369.

[6] A. Popovich, V. Sufiiarov, I. Polozov, E. Borisov, D. Masaylo, and A. Orlov, “Microstructure and mechanical properties of additive manufactured copper alloy,” *Materials Letters*, vol. 179, pp. 38–41, Sep. 2016, doi: 10.1016/j.matlet.2016.05.064.

[7] K. Jahns, R. Bappert, P. Böhlke, and U. Krupp, “Additive manufacturing of CuCr1Zr by development of a gas atomization and laser powder bed fusion routine,” *The International Journal of Advanced Manufacturing Technology*, vol. 107, no. 5–6, Art. no. 5–6, Mar. 2020, doi: 10.1007/s00170-020-04941-7.

[8] B. Buchmayr, G. Panzl, A. Walzl, and C. Wallis, “Laser Powder Bed Fusion – Materials Issues and Optimized Processing Parameters for Tool steels, AlSiMg- and CuCrZr-Alloys,” *Adv. Eng. Mater.*, vol. 19, no. 4, Art. no. 4, Apr. 2017, doi: 10.1002/adem.201600667.

[9] C. Wallis and B. Buchmayr, “Effect of heat treatments on microstructure and properties of CuCrZr produced by laser-powder bed fusion,” *Materials Science and Engineering: A*, vol. 744, pp. 215–223, Jan. 2019, doi: 10.1016/j.msea.2018.12.017.

[10] S. Zhang, H. Zhu, L. Zhang, W. Zhang, H. Yang, and X. Zeng, “Microstructure and properties in QCr0.8 alloy produced by selective laser melting with different heat treatment,” *Journal of Alloys and Compounds*, vol. 800, pp. 286–293, Sep. 2019, doi: 10.1016/j.jallcom.2019.06.018.

[11] C. Zeng *et al.*, “Effect of temperature history on thermal properties of additively manufactured C-18150 alloy samples,” *Manufacturing Letters*, vol. 28, pp. 25–29, Apr. 2021, doi: 10.1016/j.mfglet.2021.02.002.

[12] U. Holzwarth and H. Stamm, “The precipitation behaviour of ITER-grade Cu–Cr–Zr alloy after simulating the thermal cycle of hot isostatic pressing,” *Journal of Nuclear Materials*, vol. 279, no. 1, Art. no. 1, Mar. 2000, doi: 10.1016/S0022-3115(99)00285-8.

[13] A. Chbihi, X. Sauvage, and D. Blavette, “Atomic scale investigation of Cr precipitation in copper,” *Acta Materialia*, vol. 60, no. 11, Art. no. 11, Jun. 2012, doi: 10.1016/j.actamat.2012.01.038.

[14] P. Guan *et al.*, “Effect of selective laser melting process parameters and aging heat treatment on properties of CuCrZr alloy,” *Materials Research Express*, vol. 6, no. 11, Art. no. 11, Oct. 2019, doi: 10.1088/2053-1591/ab4e2f.

[15] C. Jinshui, Y. Bin, W. Junfeng, X. Xiangpeng, C. Huiming, and W. Hang, “Effect of different Zr contents on properties and microstructure of Cu-Cr-Zr alloys,” *Mater. Res. Express*, vol. 5, no. 2, Art. no. 2, Feb. 2018, doi: 10.1088/2053-1591/aaabc5.

[16] J. Chen, J. Wang, X. Xiao, H. Wang, H. Chen, and B. Yang, “Contribution of Zr to strength and grain refinement in Cu Cr Zr alloy,” *Materials Science and Engineering: A*, vol. 756, pp. 464–473, May 2019, doi: 10.1016/j.msea.2019.04.053.

[17] C. Watanabe, R. Monzen, and K. Tazaki, “Mechanical properties of Cu–Cr system alloys with and without Zr and Ag,” *Journal of Materials Science*, vol. 43, no. 3, Art. no. 3, Feb. 2008, doi: 10.1007/s10853-007-2159-8.

[18] AFNOR, Standard EN12420:2014 “Cuivre et alliages de cuivre - Pièces forgées.” 2014.

[19] P.-E. Frayssines *et al.*, “CuCrZr alloy microstructure and mechanical properties after hot isostatic pressing bonding cycles,” *Phys. Scr.*, vol. 2014, no. T159, Art. no. T159, 2014, doi: 10.1088/0031-8949/2014/T159/014018.

[20] A. D. Ivanov, A. K. Nikolaev, G. M. Kalinin, and M. E. Rodin, “Effect of heat treatments on the properties of CuCrZr alloys,” *Journal of Nuclear Materials*, vol. 307–311, pp. 673–676, Dec. 2002, doi: 10.1016/S0022-3115(02)01110-8.

[21] A. P. Zhilyaev, I. Shakhova, A. Morozova, A. Belyakov, and R. Kaibyshev, “Grain refinement kinetics and strengthening mechanisms in Cu–0.3Cr–0.5Zr alloy subjected to intense plastic deformation,” *Materials Science and Engineering: A*, vol. 654, pp. 131–142, Jan. 2016, doi: 10.1016/j.msea.2015.12.038.

[22] ISO Standard EN 6507-(1-4), “Matériaux Métalliques – Essai de dureté Vickers - Partie 1 : méthode d’essai – Partie 2 : vérification et étalonnage des machines - Partie 3 : étalonnage des blocs de référence - Partie 4 : tableaux des valeurs de dureté.”

[23] ISO Standard EN 6892-1:2019 “Matériaux métalliques - Essai de traction- Partie 1: Méthode d’essai à température ambiante.” 2019.

[24] ISO Standard EN 2004-1, “Série aérospatiale - Méthodes d’essais applicables aux produits en aluminium et alliages d’aluminium - Partie 1 : détermination de la conductivité électrique des alliages d’aluminium corroyés.” 2004.

[25] S. Gorsse, C. Hutchinson, M. Gouné, and R. Banerjee, “Additive manufacturing of metals: a brief review of the characteristic microstructures and properties of steels, Ti-6Al-4V and high-entropy alloys,” *Science and Technology of Advanced Materials*, vol. 18, no. 1, Art. no. 1, Dec. 2017, doi: 10.1080/14686996.2017.1361305.

[26] J. Metelkova, “On the influence of laser defocusing in Selective Laser Melting of 316L,” *Additive Manufacturing*, p. 9, 2018.

[27] P. Krakhmalev *et al.*, “Microstructure, Solidification Texture, and Thermal Stability of 316 L Stainless Steel Manufactured by Laser Powder Bed Fusion,” *Metals*, vol. 8, no. 8, Art. no. 8, Aug. 2018, doi: 10.3390/met8080643.

[28] S. Huang, W. Huang, W. Xie, H. Chen, H. Wang, and B. Yang, “Microstructure and strengthening mechanisms of CuCrZr alloy by two-step thermomechanical treatment,” *Journal of Materials Science: Materials in Electronics*, Sep. 2020, doi: 10.1007/s10854-020-04333-3.

[29] D. R. Lide and Chemical Rubber Company, Eds., *CRC handbook of chemistry and physics: a ready-reference book of chemical and physical data*, 90. ed., 2009–2010. Boca Raton, FLa.: CRC Press, 2009.

[30] M. Merola *et al.*, “Influence of the manufacturing heat cycles on the CuCrZr properties,” *Journal of Nuclear Materials*, vol. 307–311, pp. 677–680, Dec. 2002, doi: 10.1016/S0022-3115(02)01186-8.

[31] H. Li, S. Xie, P. Wu, and X. Mi, “Study on improvement of conductivity of Cu-Cr-Zr alloys,” *Rare Metals*, vol. 26, no. 2, Art. no. 2, Apr. 2007, doi: 10.1016/S1001-0521(07)60171-5.

[32] Z. Que, J. Lee, W. Cheng, S. Han, H. Jung, and K. Euh, “Microstructure Evolution of the Cu-Cr Hypereutectic Alloys During Directional Solidification,” in *Future Information Communication Technology and Applications: ICFICE 2013*, H.-K. Jung, J. T. Kim, T. Sahama, and C.-H. Yang, Eds. Dordrecht: Springer Netherlands, 2013, pp. 939–947. doi: 10.1007/978-94-007-6516-0_103.

[33] D. Liu, P. Wang, Y. Song, Q. Li, and J. Chen, “Effect of the ITER FW Manufacturing Process on the Microstructure and Properties of a CuCrZr Alloy,” *Plasma Sci. Technol.*, vol. 17, no. 10, Art. no. 10, Oct. 2015, doi: 10.1088/1009-0630/17/10/13.

[34] Y. Liu, Z. Li, Y. Jiang, Y. Zhang, Z. Zhou, and Q. Lei, “The microstructure evolution and properties of a Cu–Cr–Ag alloy during thermal-mechanical treatment,” *Journal of Materials Research*, vol. 32, no. 07, Art. no. 07, Apr. 2017, doi: 10.1557/jmr.2017.17.

[35] M. J. Starink and S. C. Wang, “A model for the yield strength of overaged Al–Zn–Mg–Cu alloys,” *Acta Materialia*, vol. 51, no. 17, Art. no. 17, Oct. 2003, doi: 10.1016/S1359-6454(03)00363-X.

[36] Q. Lei, Z. Li, A. Zhu, W. Qiu, and S. Liang, “The transformation behavior of Cu–8.0Ni–1.8Si–0.6Sn–0.15Mg alloy during isothermal heat treatment,” *Materials Characterization*, vol. 62, no. 9, Art. no. 9, Sep. 2011, doi: 10.1016/j.matchar.2011.06.008.

[37] J. Zhou *et al.*, “Microstructure and properties of powder metallurgy Cu-1%Cr-0.65%Zr alloy prepared by hot pressing,” *Vacuum*, vol. 131, pp. 156–163, Sep. 2016, doi: 10.1016/j.vacuum.2016.06.008.

[38] H. Feng, H. Jiang, D. Yan, and L. Rong, “Effect of continuous extrusion on the microstructure and mechanical properties of a CuCrZr alloy,” *Materials Science and Engineering: A*, vol. 582, pp. 219–224, Oct. 2013, doi: 10.1016/j.msea.2013.06.031.

[39] A. J. Ardell, “Precipitation hardening,” *METALLURGICAL TRANSACTIONS A*, p. 35, 1985.

[40] R. N. Caron, “Copper: Alloying,” in *Reference Module in Materials Science and Materials Engineering*, Elsevier, 2016, p. B9780128035818025000. doi: 10.1016/B978-0-12-803581-8.02563-7.

[41] N. Hansen, “Hall–Petch relation and boundary strengthening,” *Scripta Materialia*, vol. 51, no. 8, Art. no. 8, Oct. 2004, doi: 10.1016/j.scriptamat.2004.06.002.

[42] A. W. Thompson and W. A. Backofen, “The effect of grain size on fatigue,” *Acta Metallurgica*, vol. 19, p. 10, 1971.

[43] D. François, A. Pineau, and A. Zaoui, *Comportement mécanique des matériaux. vol. 1 vol. 1*. Paris: Hermès, 1991.

[44] T. Gladman, “Precipitation hardening in metals,” *Materials Science and Technology*, vol. 15, no. 1, Art. no. 1, Jan. 1999, doi: 10.1179/026708399773002782.

[45] R. M. Aikin and L. Christodoulou, “The role of equiaxed particles on the yield stress of composites,” *Scripta Metallurgica et Materialia*, vol. 25, no. 1, Art. no. 1, Jan. 1991, doi: 10.1016/0956-716X(91)90345-2.

[46] T. Torma, E. Kovacs-Csetenyi, T. Turmezey, T. Ungar, and I. Kovacs, “Hardening mechanisms in Al-Sc alloys,” *Journal of Materials Science*, vol. 24, no. 11, Art. no. 11, Nov. 1989, doi: 10.1007/BF01168955.

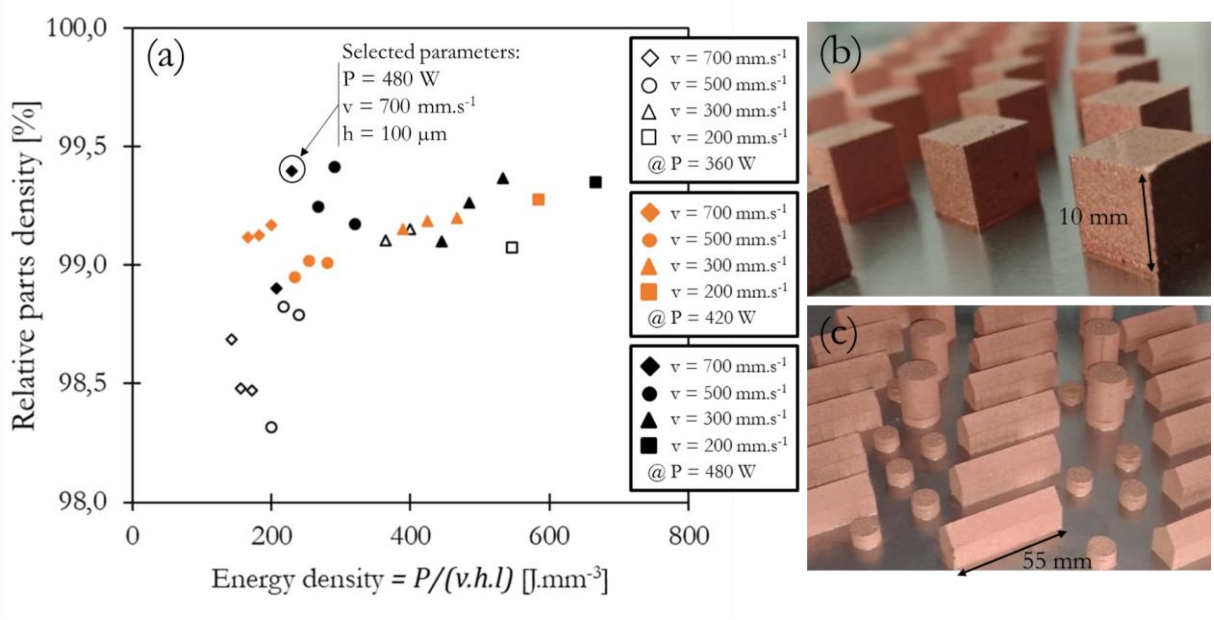

Figure 1: (a) Relative parts density (compared to CuCrZr HIPped samples density of 8.908 g.cm^{-3}) as a function of the energy density for various parameters sets. Varying scanning speed at a laser power of 360 W (white marks), 420 W (orange marks) and 480 W (black marks) using different hatch (100, 110 and 120 µm) and a layer thickness fixed at 30 µm. (b) L-PBF as-built cubes (10x10x10 mm^3) and (c) mechanical (55x13x13 mm^3 parallelepiped) and electrical samples (18 mm diameter and 22 mm high cylinder).

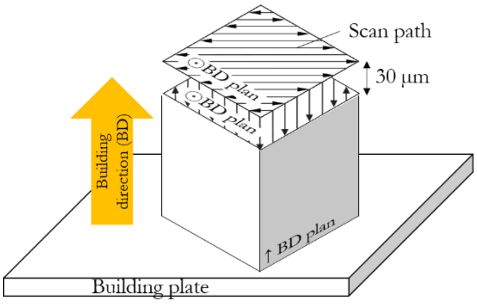

Figure 2 : Schema of the ⊙ BD plan and ↑ BD plan orientations in regard to L-PBF scan path and sample edges

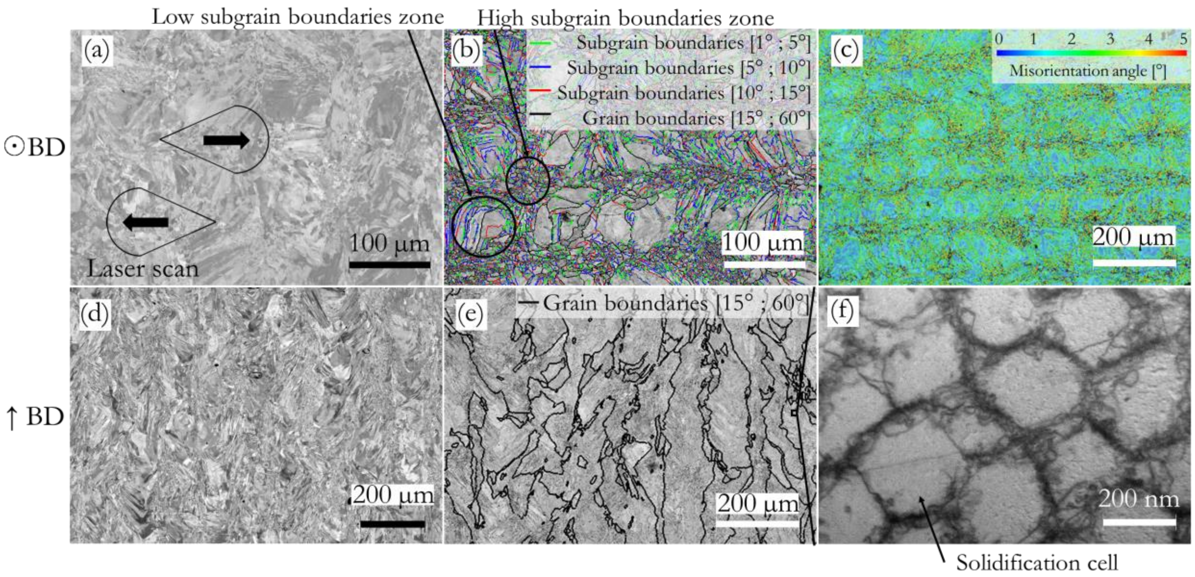

Figure 3: SEM images of as-built L-PBF CuCrZr sample in the (a) ⊙ BD and (d) ↑ BD plans, (b) quality pattern image of (a) superimposed with grain and subgrain boundaries, and (e), quality pattern image of (d) superimposed with grain boundaries only. (c) KAM map of (a) and (f) TEM image of the solidification cells.

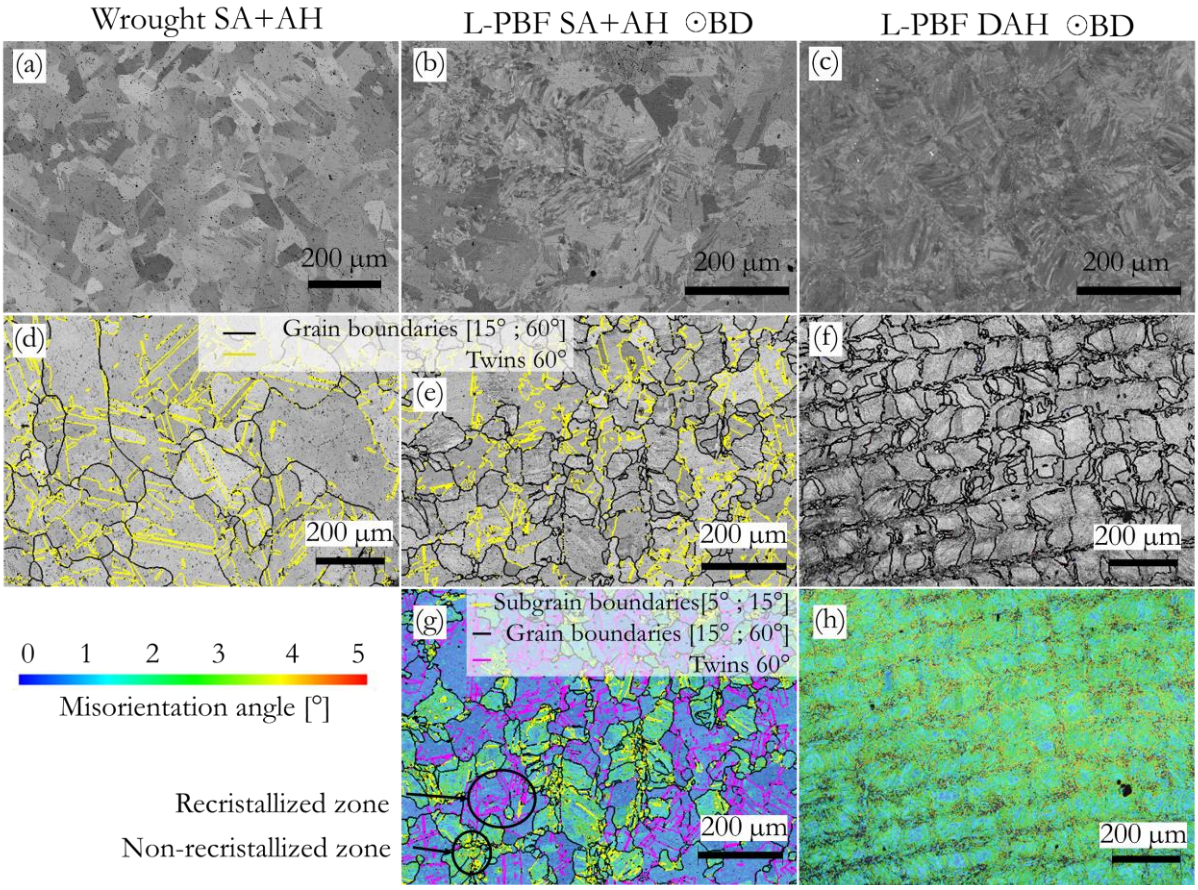

Figure 4 : SEM-EBSD analysis of the (a, d) wrought, (b, e, g) L-PBF SA+AH and (c, f, h) L-PBF DAH CuCrZr samples. (a-c) SEM images in the ⊙ BD plan; (d-f) quality pattern images with grain boundaries and twins of (a-c) respectively. (g, h) KAM analysis of respectively L-PBF SA + AH and L-PBF DAH CuCrZr in the ⊙ BD plan.

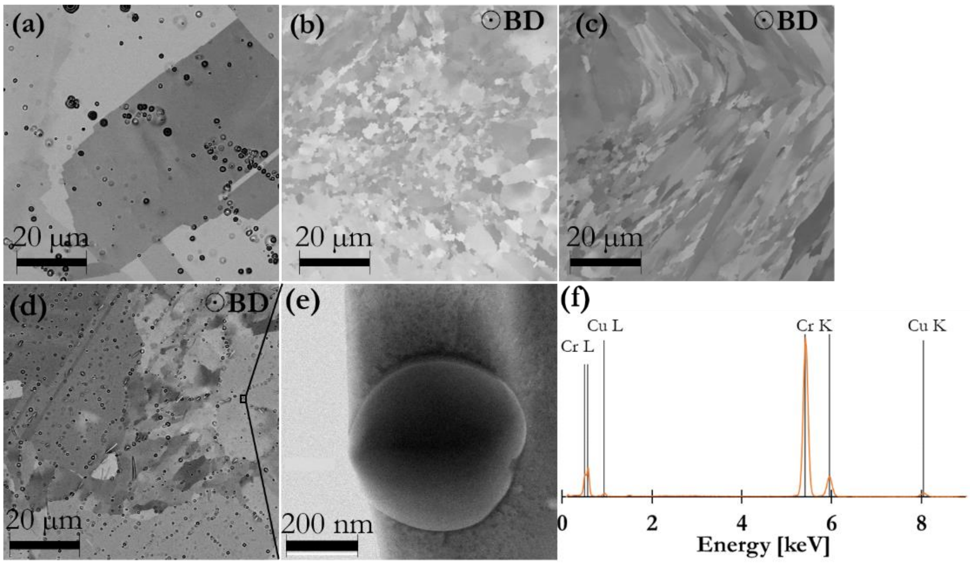

Figure 5: Study of the micro-precipitation: SEM images of (a) Wrought CuCrZr, (b) L-PBF as-built CuCrZr and (c) L-PBF DAH CuCrZr, both exempt of micro-precipitates, (d) L-PBF SA+AH CuCrZr. (e) TEM image focused on a Cr micro-precipitate, and (f) an EDX analysis of one of them.

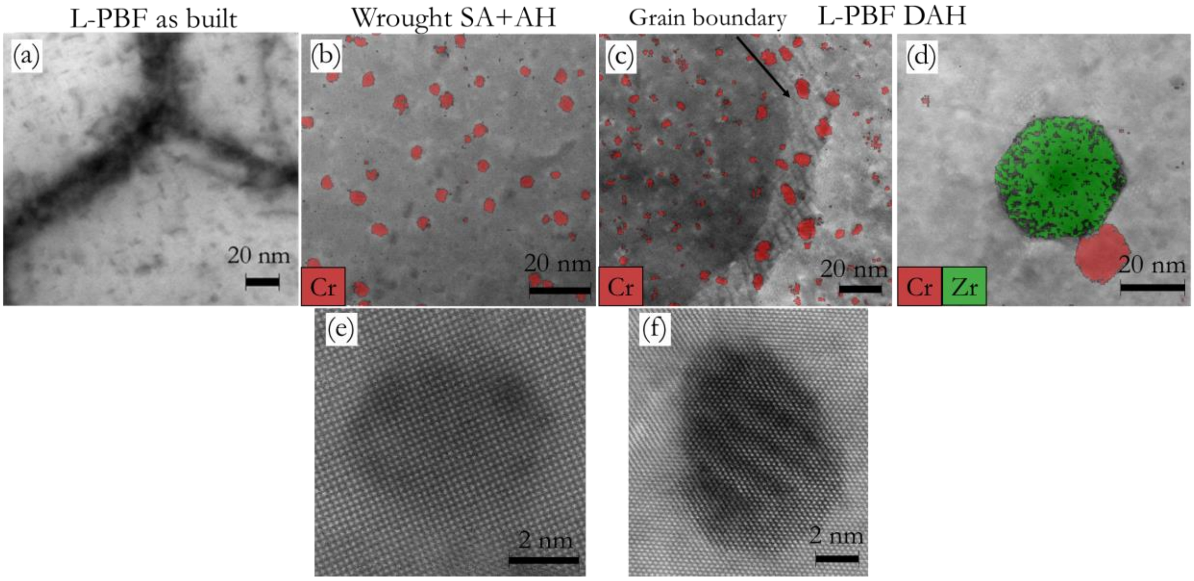

Figure 6: HAADF/STEM and Cr and Zr EDX analysis of the (a) L-PBF as built CuCrZr showing no nano-precipitates; (b, e) wrought SA+AH CuCrZr showing Cr nano-precipitation (no Zr detected; matrix is pure Cu on these images); (c, f) L-PBF DAH CuCrZr showing Cr nano-precipitation (no Zr detected; matrix is pure Cu on these images); (d) L-PBF DAH CuCrZr showing a Zr nano-precipitate next to a Cr nano-precipitate

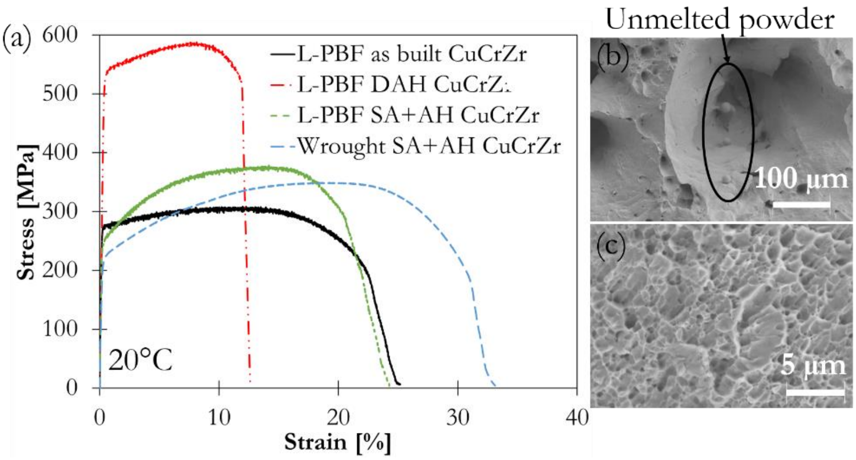

Figure 7: (a) Engineering stress-strain response of wrought SA + AH, L-PBF as-built, SA + AH and DAH CuCrZr samples at a test temperature of 20°C (as the curves were qualitatively similar, only 1 of the 3 curves obtained for each condition is shown); SEM images of tensile bars fractography of (b) L-PBF as-built CuCrZr and (c) L-PBF SA+AH CuCrZr.

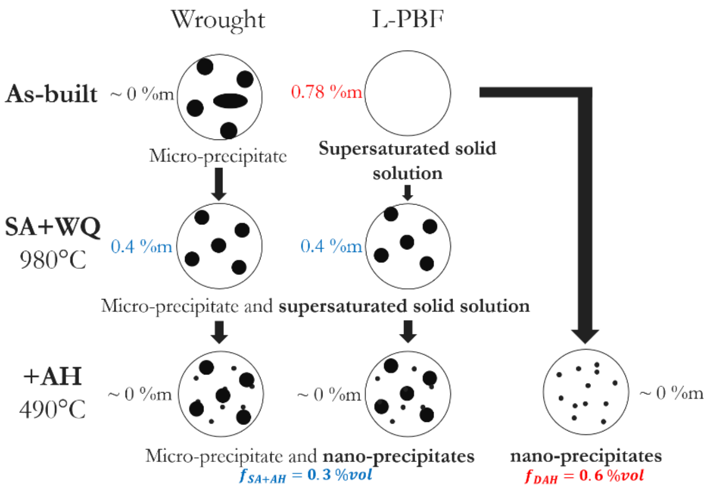

Figure 8 : Microstructural evolution of L-PBF and wrought CuCrZr as a function of the heat treatments. The Cr content in solid solution is noted next to the pictures. The final volume fractions of Cr nano-precipitates are given at the bottom.

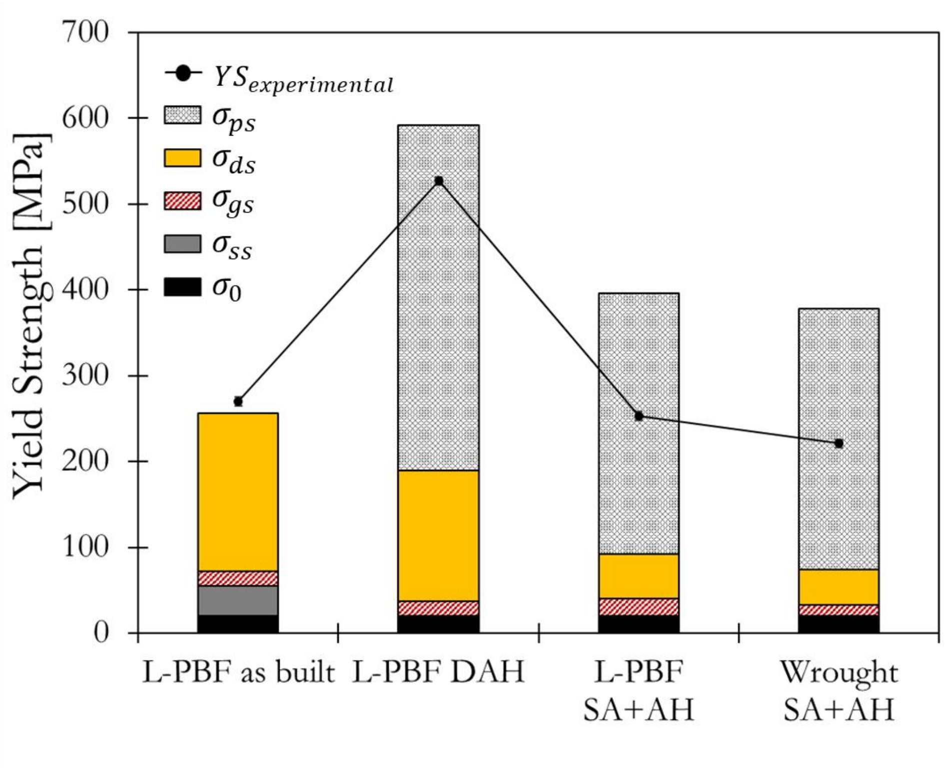

Figure 9: Calculated hardening mechanisms contributions to the yield strengths of CuCrZr alloys processed by four different routes, compared to experimental values (black spots)